

# R&D for Very Forward Calorimeters for ILC Detectors

---

H. Abramowicz<sup>a</sup>, A. Abusleme<sup>b</sup>, K. Afanaciev<sup>c</sup>, J. Aguilar<sup>i</sup>, P. Ambalathankandy<sup>i</sup>, P. Bambade<sup>o</sup>, Ivanka Bozovic-Jelisavcic<sup>d</sup>, E. Castro<sup>e</sup>, G. Chelkov<sup>f</sup>, C. Coca<sup>g</sup>, A. Dragone<sup>p</sup>, K. Elsener<sup>h</sup>, I. Emeliantchik<sup>b</sup>, T. Fiutowski<sup>i</sup>, M. Gostkin<sup>f</sup>, G. Grzelak<sup>b</sup>, G. Haller<sup>p</sup>, H. Henschel<sup>e</sup>, A. Ignatenko<sup>c</sup>, M. Idzik<sup>i</sup>, K. Ito<sup>j</sup>, T. Jovin<sup>d</sup>, E. Kielar<sup>l</sup>, J. Kotula<sup>l</sup>, Z. Krumstein<sup>f</sup>, Sz. Kulisi<sup>i</sup>, W. Lange<sup>e</sup>, W. Lohmann<sup>e\*</sup>, A. Levy<sup>a</sup>, A. Moszczynski<sup>l</sup>, U. Nauenberg<sup>k</sup>, O. Novgorodova<sup>e</sup>, M. Ohlerich<sup>e</sup>, G. Oleinik<sup>k</sup>, K. Oliwa<sup>l</sup>, A. Olshevski<sup>f</sup>, M. Pandurovic<sup>d</sup>, B. Pawlik<sup>l</sup>, D. Przyborowski<sup>i</sup>, Y. Sato<sup>j</sup>, I. Sadeh<sup>a</sup>, A. Sailer<sup>h</sup>, R. Schmidt<sup>e</sup>, B. Schumm<sup>m</sup>, S. Schuwalow<sup>e</sup>, I. Smiljanic<sup>d</sup>, K. Swientek<sup>i</sup>, Y. Takubo<sup>j</sup>, E. Teodorescu<sup>g</sup>, W. Wierba<sup>l</sup>, H. Yamamoto<sup>j</sup>, L. Zawiejski<sup>l</sup> and J. Zhang<sup>n</sup>

<sup>a</sup>*Tel Aviv University, Tel Aviv, Israel*

<sup>b</sup>*Stanford University, Stanford, USA*

<sup>c</sup>*NCPHEP, Minsk, Belarus*

<sup>d</sup>*Vinca Institute of Nuclear Sciences, University of Belgrade, Serbia*

<sup>e</sup>*DESY, Zeuthen, Germany*

*E-mail: Wolfgang.Lohmann@desy.de*

<sup>f</sup>*JINR, Dubna, Russia*

<sup>g</sup>*IFIN-HH, Bucharest, Romania*

<sup>h</sup>*CERN, Geneva, Switzerland*

<sup>i</sup>*AGH University of Science & Technology, Cracow, Poland*

<sup>j</sup>*Tohoku University, Sendai, Japan*

<sup>k</sup>*University of Colorado, Boulder, USA*

<sup>l</sup>*INP PAN, Cracow, Poland*

<sup>m</sup>*UC California, Santa Cruz, USA*

<sup>n</sup>*ANL, Argonne, USA*

<sup>o</sup>*Laboratoire de l'Accélérateur Linéaire, Orsay, France*

<sup>p</sup>*SLAC, Menlo Park, USA*

**ABSTRACT:** Special calorimeters are needed to instrument the very forward region of an ILC detector. These devices will improve the hermeticity being important for new particle searches. A luminometer is foreseen to measure the rate of low angle Bhabha scattering with a precision better than  $10^{-3}$ . A calorimeter adjacent to the beam-pipe will be hit by a large amount of beamstrahlung remnants. The amount and shape of these depositions will allow a fast luminosity estimate and the determination of beam parameters. However, the sensors must be extremely radiation hard. Finely segmented and very compact calorimeters will match the requirements. Due to the high occupancy fast front-end electronics is needed. The design of the calorimeters developed and optimised with Monte Carlo simulations is presented. Sensors and readout electronics ASICS have been designed and prototypes are available. Results on the performance of these major components are summarised.

**KEYWORDS:** Forward Calorimeters, ILC Detector, Luminosity Measurement .

---

\*Corresponding author.

---

## Contents

<b>1. Challenges</b>	<b>2</b>
<b>2. Design of the Very Forward Region</b>	<b>3</b>
2.1 LumiCal Simulation Studies	3
2.2 BeamCal Simulation Studies	6
2.3 Pair Monitor Simulations	8
<b>3. Mechanics</b>	<b>9</b>
<b>4. Systematic Effects in the Luminosity Measurement</b>	<b>10</b>
4.1 Beam-Beam Interaction	11
4.2 Background from Four-fermion Production	11
4.3 Effects of a Bias in the Energy Resolution and the Energy Scale	12
4.4 Impact of Electron and Positron Polarisation	13
4.5 Summary of Systematic Uncertainties	13
<b>5. Sensor Development</b>	<b>13</b>
5.1 BeamCal	13
5.1.1 GaAs Sensors	14
5.1.2 CVD Diamond Sensors	15
5.2 Sensors for LumiCal	15
<b>6. ASIC Developments</b>	<b>16</b>
6.1 LumiCal Readout	16
6.1.1 Front-end Electronics Design	17
6.1.2 Front-end Electronics Measurements	18
6.1.3 ADC Design	19
6.1.4 ADC Performance Measurements	19
6.2 BeamCal Front-End ASIC Development	20
6.2.1 Circuit Implementation	21
6.2.2 Test Results	22
6.3 Pair Monitor	23
<b>7. Acknowledgments</b>	<b>24</b>

## 1. Challenges

Two specialised calorimeters are foreseen in the very forward region of the ILC detector - LumiCal for the precise measurement of the luminosity and BeamCal for a fast estimate of the luminosity and to control beam parameters [1]. Both will also improve the hermeticity of the detector. To support beam-tuning a pair-monitor will be positioned just in front of BeamCal.

LumiCal will measure the luminosity using Bhabha scattering,  $e^+e^- \rightarrow e^+e^-(\gamma)$ , as a gauge process. To match the physics benchmarks, an accuracy of better than  $10^{-3}$  is needed at a centre-of-mass energy of 500 GeV [2]. For the GigaZ option, an accuracy of  $10^{-4}$  would be required [3]. To ensure these accuracies, a precision device is needed, with particularly challenging requirements on the mechanics and position control.

BeamCal is positioned just outside the beam-pipe. A large amount of low energy electron-positron pairs originating from beamstrahlung will deposit their energy in BeamCal. These depositions, useful for a bunch-by-bunch luminosity estimate and the determination of beam parameters [4], will lead, however, to a radiation dose of several MGy per year in the sensors at lower polar angles. Hence radiation hard sensors are needed to instrument BeamCal. A pair monitor, consisting of a layer of pixel sensors positioned just in front of BeamCal, will measure the density of beamstrahlung pairs and give additional information for the beam parameter determination.

All detectors in the very forward region have to tackle relatively high occupancy, requiring special front-end (FE) electronics.

A small Moliere radius is of importance for both calorimeters. It ensures high energy electron veto capability for BeamCal even at small polar angles, being essential to suppress background in searches for new particles where the signature is large missing energy and momentum. In LumiCal the precise reconstruction of electron and positron showers of Bhabha events is facilitated.

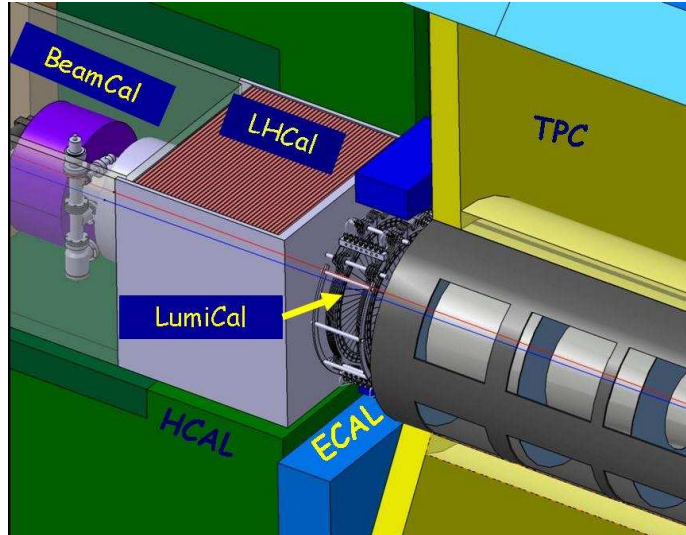


Figure 1: The very forward region of the ILD detector. LumiCal, BeamCal and LHCAL are carried by the support tube for the final focusing quadrupole and the beam-pipe. TPC denotes the central track chamber, ECAL the electromagnetic and HCAL the hadron calorimeter.

## 2. Design of the Very Forward Region

A sketch of the very forward region of the ILD detector [2], as an example, is shown in Figure 1. LumiCal and BeamCal are designed as cylindrical sensor-tungsten sandwich electromagnetic calorimeters. Both consist of 30 absorber disks of 3.5 mm thickness, each corresponding to one radiation length, interspersed with sensor layers. Each sensor layer is segmented radially and azimuthally in pads. Front-end ASICs are positioned at the outer radius of the calorimeters. LumiCal is positioned inside and aligned with the end-cap electromagnetic calorimeter. BeamCal is placed just in front of the final focus quadrupole. BeamCal covers polar angles between 5 and 40 mrad and LumiCal between 31 and 77 mrad.

Colliding beams enter the interaction point, IP, with a crossing angle of 14 mrad. Both calorimeters are centered around the outgoing beam. In the design of BeamCal a hole for the incoming beam-pipe is foreseen.

### 2.1 LumiCal Simulation Studies

The cross section of Bhabha scattering can be calculated precisely from theory. In leading order it reads:

$$\frac{d\sigma_B}{d\theta} = \frac{2\pi\alpha_{em}^2}{s} \frac{\sin\theta}{\sin^4(\theta/2)} \approx \frac{32\pi\alpha_{em}^2}{s} \frac{1}{\theta^3}, \quad (2.1)$$

where  $\theta$  is the polar angle of the scattered electron with respect to the beam. The approximation holds at small  $\theta$ .

Counting the number of Bhabha events,  $N_B$ , in a certain  $\theta$ -range, the luminosity,  $L$ , is obtained as:

$$L = \frac{N_B}{\sigma_B}. \quad (2.2)$$

Because of the steep  $\theta$  dependence of the cross section, as illustrated in Figure 2a, the most critical quantity to control when counting Bhabha events is the inner acceptance radius of the calorimeter, defined as the lower cut in the polar angle. Hence we need a very precise  $\theta$  measurement. Furthermore, the  $\theta$ -range must be chosen such that the amount of Bhabha events measured ensures the necessary statistical accuracy. Choosing the lower bound of the polar angle between 40 and 60 mrad the latter requirement can be easily reached, as illustrated in Figure 2b. Here a Bhabha event sample generated with the BHWIDE generator [5] is used.

Electromagnetic showers are simulated in LumiCal using the GEANT4 [6] based package Mokka [7]. The depositions in each sensor pad are recorded, and a reconstruction of the shower is performed. The position of an electromagnetic shower in LumiCal is reconstructed by performing a weighted average over the depositions on individual pads. The weight,  $\mathcal{W}_i$ , of a given detector pad  $i$  is determined by logarithmic weighting [8], for which  $\mathcal{W}_i = \max\{0, \mathcal{C} + \ln(E_i/E_{tot})\}$ . Here  $E_i$  refers to the individual pad energy,  $E_{tot}$  is the total energy in all pads, and  $\mathcal{C}$  is a constant. In this way, only pads which contain a sufficient fraction of the shower energy contribute to the reconstruction. The polar angle resolution,  $\sigma_\theta$ , and a polar angle measurement bias,  $\Delta\theta$ , are defined as the Gaussian width and the central value of the difference between the reconstructed and the generated polar angles. There is an optimal value for  $\mathcal{C}$ , for which  $\sigma_\theta$  is minimal [9, 10].

Non-zero values of  $\Delta\theta$  are due to the non-linear signal sharing on finite size pads with gaps between them. The bias and the resolution in the polar angle measurement depend on the polar

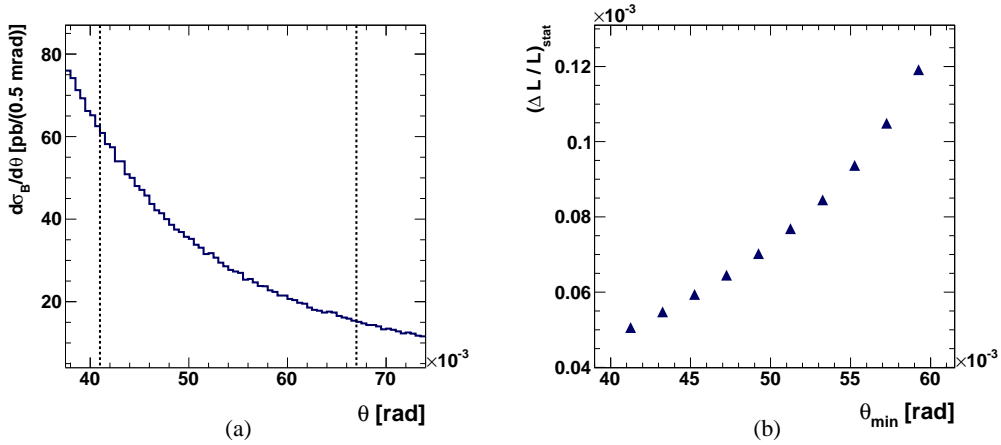


Figure 2: (a) Dependence of  $d\sigma_B/d\theta$ , the differential Bhabha cross-section, on the polar angle,  $\theta$ , at  $\sqrt{s} = 500$  GeV. The dashed lines mark the fiducial volume of LumiCal,  $41 < \theta^f < 67$  mrad. (b) Dependence of the statistical uncertainty in counting the number of Bhabha events,  $(\Delta L/L)_{\text{stat}}$ , on the minimal polar angle,  $\theta_{\text{min}}$ , which defines the lower edge of the fiducial volume. The upper limit is kept at 67 mrad.

angle pad size. The bias causes a shift in the luminosity measurement, since events may migrate into or out of the fiducial volume. This shift is expressed as

$$\left(\frac{\Delta L}{L}\right)_{\text{rec}} \approx 2 \frac{\Delta\theta}{\theta_{\text{min}}^f}. \quad (2.3)$$

Figure 3a shows the relative shift in the luminosity as a function of the polar angular pad size,  $l_\theta$ , using the optimal value of  $\mathcal{C}$ . For  $l_\theta < 2$  mrad the shift in the luminosity measurement is smaller than  $10^{-3}$ . As the baseline for the design we have chosen  $l_\theta = 0.8$  mrad, which corresponds to 64 radial divisions of the sensor. For this segmentation the polar angle resolution and bias amount to  $\sigma_\theta = (2.2 \pm 0.01) \times 10^{-2}$  and  $\Delta\theta = (3.2 \pm 0.1) \times 10^{-3}$  mrad, respectively. The relative shift in the luminosity is  $(\Delta L/L)_{\text{rec}} = 1.6 \times 10^{-4}$ .

The polar angle bias needs careful understanding by test-beam measurements using sensors finally chosen for the calorimeter. Once its value is known, a correction can be applied to the luminosity measurement. The uncertainty of the luminosity measurement is then given by the uncertainty of the measured bias which may be smaller than the shift itself. The value of  $1.6 \times 10^{-4}$  can therefore be considered as an upper bound on the relative luminosity bias.

Using 30 radiation length of tungsten as an absorber high energy electrons and photons deposit almost all of their energy in the detector. Defining fiducial cuts on the minimal and maximal reconstructed polar angles of the particles used for the luminosity measurement prevents events with shower leakage through the edges of LumiCal.

The relative energy resolution,  $\sigma_E/EE$ , is usually parametrized as

$$\frac{\sigma_E}{E} = \frac{a_{\text{res}}}{\sqrt{E_{\text{beam}} \text{ (GeV)}}}, \quad (2.4)$$

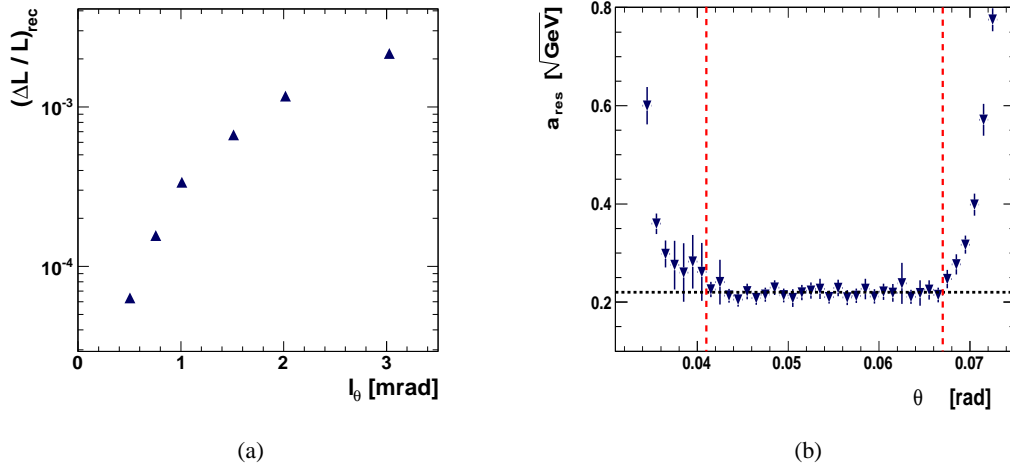


Figure 3: (a) Dependence of  $(\Delta L/L)_{\text{rec}}$ , as defined in Eqn. (2.3) on the polar angle pad size,  $l_\theta$ . (b) The energy resolution,  $a_{\text{res}}$ , for 250 GeV electrons as a function of the polar angle,  $\theta$  covering the polar angle range of the LumiCal.

where  $E$  and  $\sigma_E$  are, respectively, the central value and the standard deviation of the distribution of the energy deposited in the sensors for a beam of electrons with energy  $E_{\text{beam}}$ . The parameter  $a_{\text{res}}$  is usually quoted as the energy resolution, a convention which will be followed here.

Figure 3b shows the energy resolution as a function of the polar angle  $\theta$  for electron showers with energy 250 GeV. The energy resolution parameter approaches minimal constant values between  $\theta_{\text{min}} = 41$  mrad and  $\theta_{\text{max}} = 67$  mrad, where the shower is fully contained inside the calorimeter. The fiducial volume of LumiCal is thus defined to be the polar angular range

$$41 < \theta^f < 67 \text{ mrad.} \quad (2.5)$$

Using only electron showers inside the fiducial volume of LumiCal, the energy resolution is estimated to be  $a_{\text{res}} = 0.21 \pm 0.02 \sqrt{\text{GeV}}$ . No dependence on the electron energy is found in the energy range from 50 to 300 GeV. In order to determine the energy of showering particles, the integrated deposited energy in the detector has to be multiplied by a calibration factor. Here the calibration factor is found to be constant in the same energy range.

For the chosen segmentation of about  $300 \mu\text{m}$  thick silicon sensors the expected range of energy depositions in the pads was studied for the passage of minimum ionizing particles (MIPs) and for showers of 250 GeV electrons [11]. The energy deposition was converted to released ionisation charge. The distribution of the charge in a single pad,  $C_{\text{pad}}$ , is shown in Figure 4a. It ranges between  $4 < C_{\text{pad}} < 6 \times 10^3$  fC. The distribution of the maximal charge collected in a single pad is shown in Figure 4b. About 95 % of electron showers signals are less than  $5.4 \times 10^3$  fC.

The impact of the digitisation of the detector signal on the LumiCal performance was investigated in Ref. [11]. It was shown that an ADC with 8 bits resolution is sufficient to keep the energy

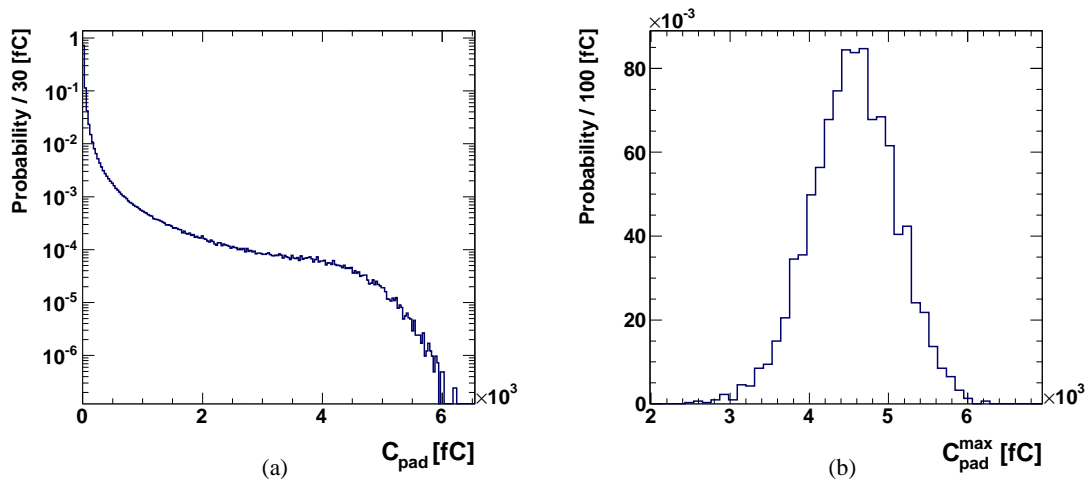


Figure 4: (a) Normalized distribution of the charge deposited in a detector pad,  $C_{\text{pad}}$ , by 250 GeV electron showers. (b) Normalized distribution of the maximal charge collected in a single pad per shower,  $C_{\text{pad}}^{\text{max}}$ , for 250 GeV electron showers.

resolution quoted above. No bias in the energy measurement is found.

## 2.2 BeamCal Simulation Studies

BeamCal will be hit after each bunch-crossing by a large amount of beamstrahlung pairs. Their number, energy and spatial distribution depends on the beam parameters and the magnetic field inside the detector. Using the nominal ILC beam-parameter set [12], beamstrahlung pairs are generated with the GUINEA-PIG program [13]. Inside the ILC detector an anti-DID field [14] is assumed. Beamstrahlung pairs are simulated in the detector, using a program based on GEANT4.

The energy depositions in BeamCal per bunch crossing, up to several TeV as shown in Figure 5a, and the shape of these depositions allow a bunch-by-bunch luminosity estimate and the determination of beam parameters with accuracies better than 10% [4].

For search experiments it is of interest to detect single high energy electrons on top of the wider spread beamstrahlung pairs. Superimposed on the pair depositions in Figure 5a is the local deposition of one high energy electron, seen as the red spot at the right side. Using an appropriate subtraction of the pair depositions and a shower-finding algorithm which takes into account the longitudinal shower profile, the deposition of the high energy electron can be detected with high efficiency, as shown in Figure 5b. This feature allows to suppress the background from two-photon processes in a search e.g. for super-symmetric tau-leptons [15] in a large fraction of the parameter space.

GEANT4 simulations are also used to determine the electromagnetic dose and the neutron fluence in the sensors after one year of operation with nominal beam parameters. The electromagnetic dose as a function of the radius in the sensor layer with the largest depositions is shown in Figure 6a. In the innermost ring of the calorimeter a dose of about 0.5 MGy is expected. Since the dose is non-uniformly distributed as a function of the azimuthal angle, it approaches 1 MGy per year in some sensor areas of the inner rings.

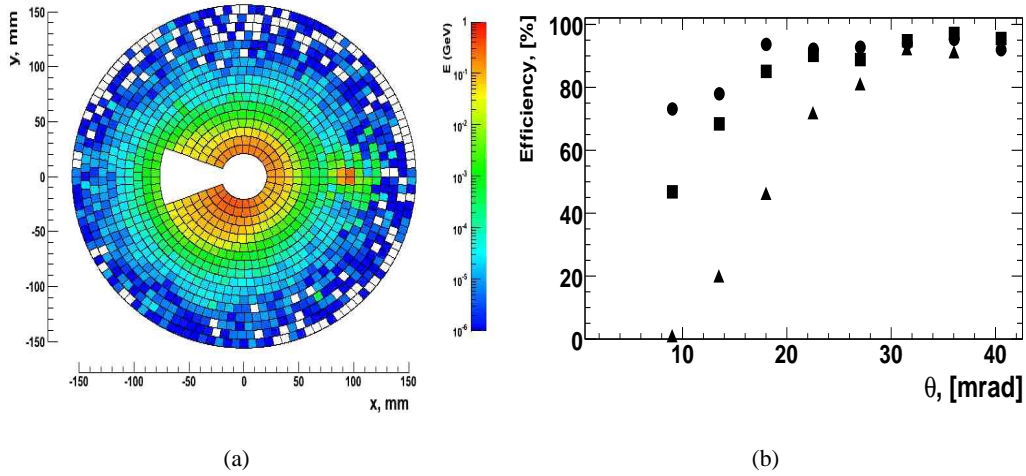


Figure 5: (a) The distribution of depositions of beamstrahlung pairs after one bunch crossing on BeamCal. Superimposed is the deposition of a single high energy electron (red spot at the right side). The white area in the center allows space for the beam-pipes. (b) The efficiency to detect single high energy electrons on top of the beamstrahlung background for electron energies of 75 (triangles), 150 (squares) and 250 (circles) GeV.

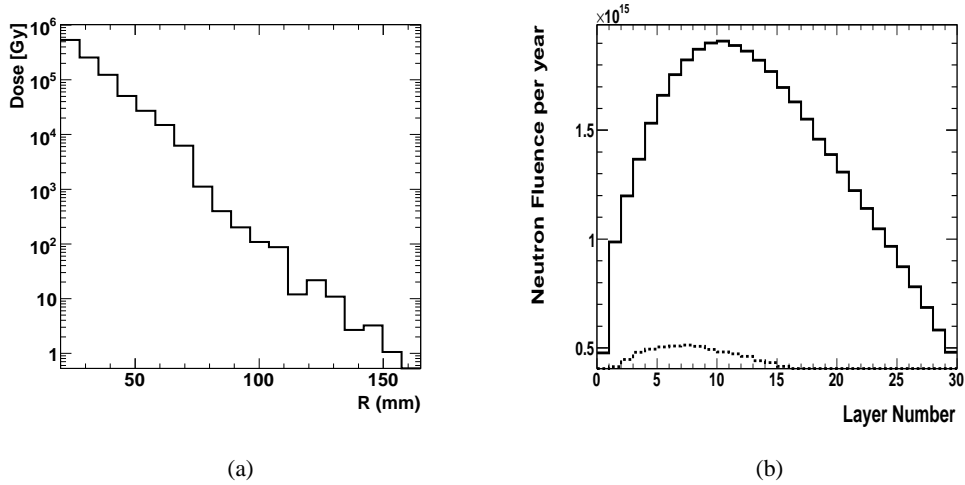


Figure 6: (a) The dose in BeamCal sensors in MGy per year as a function of the radial distance from the beam. (b) The fluence of neutrons per year inside the sensors of BeamCal as a function of the sensor layer number using the cascade model of Bertini (full line) and the standard physics list (dashed line).

The neutron fluence is estimated using two different physics lists in GEANT4. The first is the standard electromagnetic shower simulation extended by electro- and photo-nuclear interac-

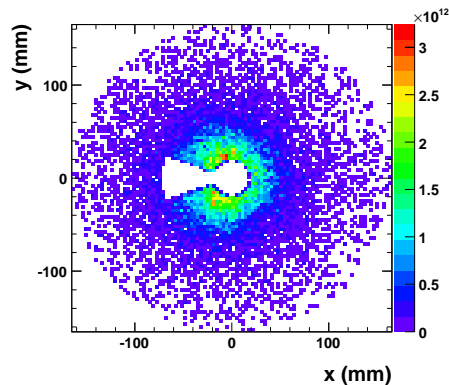


Figure 7: The fluence of neutrons per  $3 \times 3 \text{ mm}^2$  and year crossing a sensor of BeamCal with energies below 1 MeV using the list with the cascade model of Bertini.

tions, and the second the specifically designed for describing neutron interactions using the cascade model of Bertini [16]. Substantial differences, in particular in the fluence of low energy neutrons, are found, as can be seen in Figure 6b. The maximum of the neutron fluence is by a factor of 4 larger in the second model. In addition the maximum is shifted deeper into the calorimeter and the distribution is wider. At higher neutron energies the neutron spectra of both physics lists are comparable [17].

The radial distribution of low-energy neutrons in a sensor layer is shown in Figure 7 for one year of operation at nominal beam parameters. Using the cascade model of Bertini a neutron fluence of  $0.4 \times 10^{12}$  neutrons per  $\text{mm}^2$  and year is expected near the beam-pipe.

### 2.3 Pair Monitor Simulations

The pair monitor will consist of one layer of silicon pixel sensors, with pixel size of  $400 \times 400 \mu\text{m}^2$ , just in front of BeamCal to measure the number density distribution of beamstrahlung pairs. This distribution carries information on the bunch profile [18, 19]. Here we investigated the sensitivity to the horizontal and vertical bunch sizes,  $\sigma_x$  and  $\sigma_y$ , and the ratio of the vertical displacement between bunches crossing to their vertical size,  $\Delta_y$ .

To reconstruct the beam profile several observables characterising the number density of pairs at the front face of BeamCal are used [20]. Bunch crossings are simulated for certain ranges of  $\sigma_x$ ,  $\sigma_y$  and  $\Delta_y$ , and then each of these observables is fitted with a second order polynomial. Then, bunch crossings are generated using a certain set of beam parameters and  $\sigma_x$ ,  $\sigma_y$ , and  $\Delta_y$  are reconstructed with the inverse matrix method. Figure 8 shows the difference between the beam parameters reconstructed and set in the simulation divided by the latter, averaged over 50 bunch crossings. These quantities are compatible with zero, and the relative uncertainties of the horizontal and vertical beam sizes and the relative vertical displacement are given in Table 1.

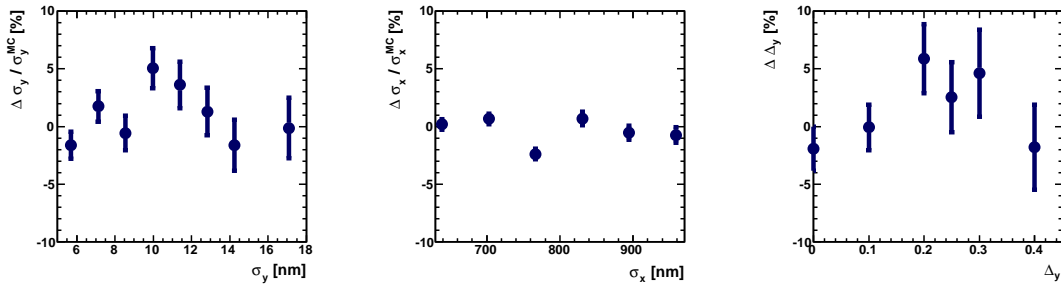


Figure 8: The relative deviations of the horizontal and vertical beam size, and the ratio of vertical displacement to the vertical beam size for 50 bunch crossings which are measured by pair monitor.

$\sigma_x$	$\sigma_y$	$\Delta_y$
3.2%	10.1%	8.0%

Table 1:

The estimated measurement accuracy of the horizontal ( $\sigma_x$ ) and vertical beam size ( $\sigma_y$ ), and ratio of vertical displacement to the vertical beam size ( $\Delta_y$ ) measured with the pair monitor.

### 3. Mechanics

On the basis of the simulation results mechanical designs of both calorimeters are developed. To allow their installation after the beam-pipe is in place both calorimeters consist of two half-cylinders. A schematic of a half cylinder of BeamCal is shown in Figure 9a. The tungsten absorber disks are

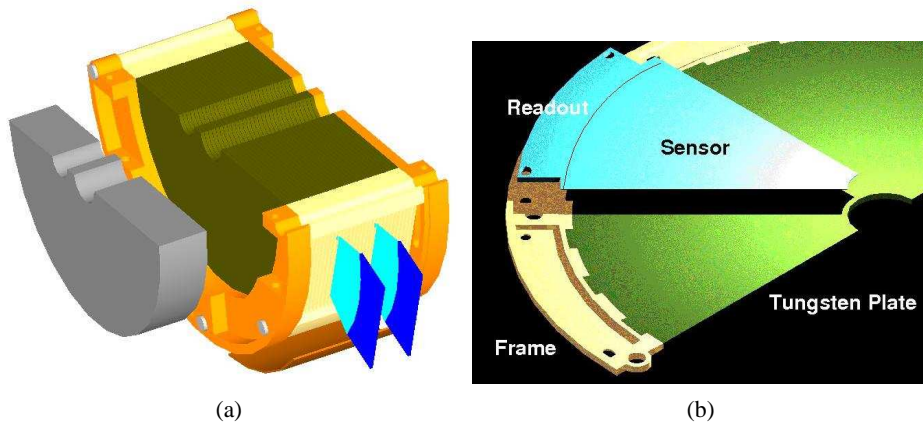


Figure 9: (a) A half-cylinder of BeamCal. The brown block is the tungsten absorber structure interspersed with sensor layers. The orange structure represents the mechanical frame. The blue segments at the outer radius indicate the front-end electronics. In front of the calorimeter a graphite shield is shown in gray. (b) A half-layer of an absorber disk assembled with a sensor sector and the front-end read-out.

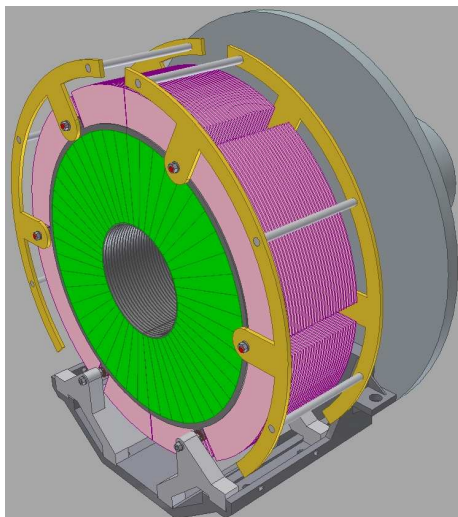


Figure 10: The mechanical structure of LumiCal. Tungsten disks are precisely positioned using 4 bolts which are stabilized by additional steel rings on both sides of the cylinder.

embedded in a mechanical frame stabilised by steel rods. Each layer is composed of the tungsten half-disc surrounded by a brass half-ring as shown in Figure 9b. Precise holes in the brass ring will ensure the necessary position accuracy. The sensors are fixed on the tungsten and connected via a flexible PCB to the front-end readout. The distance between two adjacent tungsten plates is kept just below 1 mm to ensure the smallest possible Moliere radius. The sensors of BeamCal are structured into pads of about  $8 \times 8 \text{ mm}^2$  size allowing the maximum electron detection efficiency [21]. Due to the required high radiation tolerance, GaAs sensors are foreseen. For the innermost part of BeamCal, adjacent to the beam-pipes, also CVD diamond is considered.

The design of LumiCal is similar [22]. Since it is a precision device special care is devoted to the mechanical stability and position control. The tungsten half-discs are held by special bolts. For a half barrel structure as shown in Figure 10 a finite element simulation is performed. The calorimeter weight leads to a maximal vertical displacement of  $20 \mu\text{m}$ . For a temperature difference of one degree Kelvin over a disk the deformation of the shape of the tungsten plate is estimated to be  $25 \mu\text{m}$ . For LumiCal sensors made of high ohmic n-type silicon are foreseen. The thickness of the sensors is  $300 \mu\text{m}$ . The  $p^+$  side is segmented in polar and azimuthal pads and the backside is fully metalized. To keep the Moliere radius small the gap for the sensors is 1 mm.

The signals on the pads of both calorimeters are lead by thin copper strips on a Kapton PCB to the FE electronics positioned at the outer radius of the calorimeter.

#### 4. Systematic Effects in the Luminosity Measurement

Several phenomena which may have an impact on the luminosity measurement are considered here, and methods how to control their impact are described. These are: pinch effect and beamstrahlung, background from 2-photon processes, the resolution and scale of the electron energy measurement and the beam polarisations.

## 4.1 Beam-Beam Interaction

The acceleration of electrons and positrons towards the bunch center when bunches are crossing changes their momentum, and electrons and positrons radiate beamstrahlung prior to Bhabha scattering. In addition, final state particles are deflected inside the bunch. The result is a reduction of the Bhabha counting rate in a given range of low polar angles. This reduction is found to depend on the selection criteria for Bhabha events, and amounts for a certain selection to  $1.51 \pm 0.05\%$  [23] using nominal ILC beam parameters at 500 GeV centre-of-mass energy. The uncertainty stems from the statistics in the simulation. The dominant contribution to the loss is due to beamstrahlung reducing the centre-of-mass energy, leading to an effective centre-of-mass energy distribution called luminosity spectrum.

In the measurement of the luminosity, the loss of Bhabha events has to be corrected for. The impact of beamstrahlung can be estimated from the measured luminosity spectrum with a relative uncertainty of about  $10^{-3}$ . The impact of the deflection inside the bunch depends mainly on the horizontal bunch-size,  $\sigma_x$ , and the bunch length,  $\sigma_z$ . Assuming that one can control these two quantities with a relative uncertainty of 5% [4], the uncertainty of an correction to the luminosity is about  $1.5 \times 10^{-3}$ .

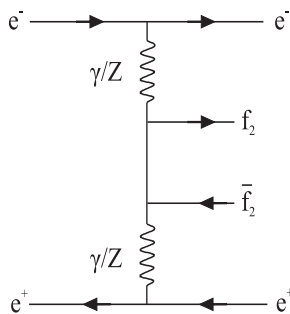


Figure 11: The Feynman graph for the dominant process in four-fermion production.

## 4.2 Background from Four-fermion Production

Four-fermion production is known to have a large cross section with maxima at low polar angles.

It is dominated by a diagram as shown in Figure 11, where two virtual photons are exchanged between electron spectators. We used the WHIZARD [24] event generator to obtain samples of events for final states with leptons in the inner legs. The generator was tuned to experimental data of the process  $e^+e^- \rightarrow e^+e^- c\bar{c}$  using data from LEP and other accelerators [25]. The cross-section of four-fermion production amounts to  $12.0 \pm 0.5$  nb at 500 GeV when the momenta of the exchanged photons are required to be larger than 0.1 GeV/c. The spectators remain at high energy. Less than 1% of them hit the luminosity calorimeter and become a background for Bhabha events. A Bhabha event sample has been generated with a cross-section of  $4.70 \pm 0.03$  nb at 500 GeV centre-of-mass energy, using the BHLUMI [26] event generator. The LumiCal response is simulated using BARBIE V4.3 [27], a GEANT3 based simulation program. The following event selection criteria are applied: the polar angle of the reconstructed shower must be within the LumiCal fiducial volume at one side and within  $\theta_{min} + 4$  mrad and  $\theta_{max} - 7$  mrad on the other. In addition, the total

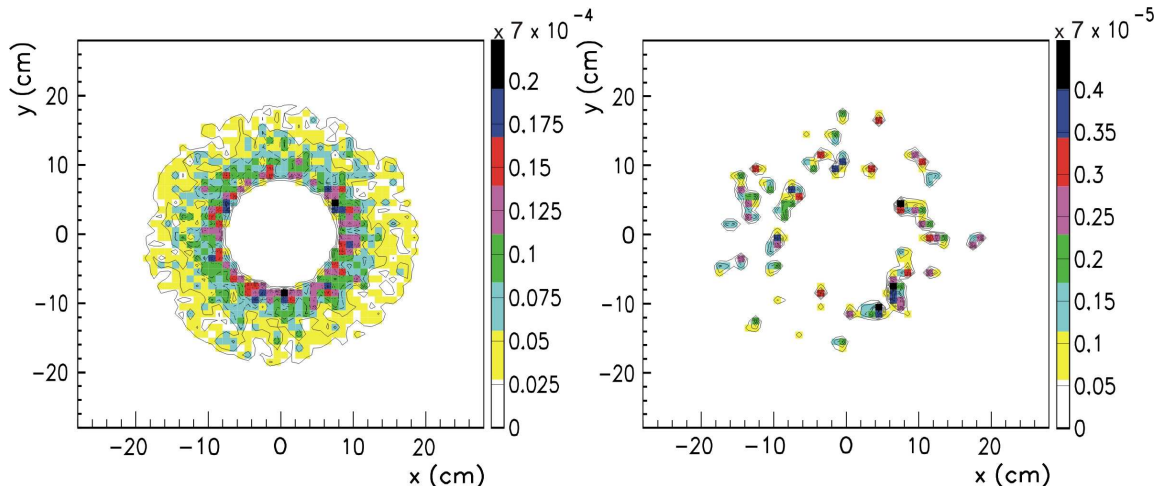


Figure 12: Hits originating from four-fermion interactions per bunch crossing on the first plane of LumiCal at 500 GeV, before (left) and after (right) application of Bhabha event selection criteria.

energy deposited in both calorimeters must be more than 80% of the center-of-mass energy. These criteria reduce the impact of beamstrahlung and deflection to the value given above [23]. The selection efficiency is about 68%.

Four-fermion events in the LumiCal are to a large fraction rejected by the Bhabha selection criteria. This is illustrated in Figure 12 where the hits of particles from the four-fermion final states in the front plane of LumiCal are shown before and after applying the Bhabha event selection. The fraction of four-fermion final states in the selected Bhabha event sample is  $2.3 \times 10^{-3}$ .

At LEP energies agreement between measurements and modeling of four-fermion processes was obtained within 20% [25]. Assuming conservatively that at 500 GeV these processes will be described within 40% a correction with an uncertainty of  $0.9 \times 10^{-3}$  can be applied to the measured luminosity.

### 4.3 Effects of a Bias in the Energy Resolution and the Energy Scale

One of the criteria to select Bhabha events is the total energy measured in the calorimeters to be larger than 80% of the centre-of-mass energy. A possible bias in the energy resolution or the energy calibration will result in a change of the number of selected Bhabha events and hence in the measured luminosity.

The selection efficiency for Bhabha events as a function of the required energy in the calorimeters is shown in Figure 13a. At the position of the cut in the measured calorimeter energy the slope of the tangent to the function is about  $-1.8 \times 10^{-3}$ . To keep the shift of the luminosity below  $10^{-3}$ , the cut in the measured calorimeter energy must be controlled with a precision of about 400 MeV. A study done allowing a constant offset in the measured energy leads to a similar requirement [28].

The effect of a bias in the energy resolution,  $a_{\text{res}}$  in Eqn. (2.4), is illustrated in Figure 13b. We estimate that  $a_{\text{res}}$  can be controlled to about 10%, contributing to the luminosity uncertainty with about  $3 \times 10^{-4}$ .

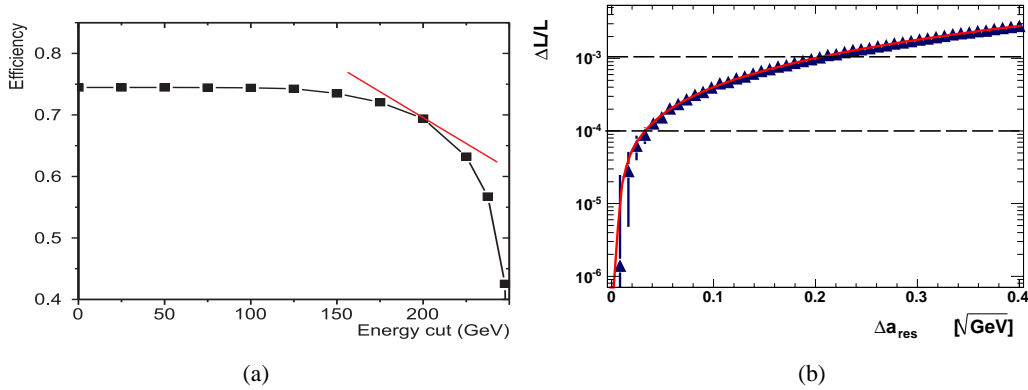


Figure 13: (a) The selection efficiency for Bhabha events as a function of the measured shower energy, (b) The shift of the measured luminosity as a function of the bias in the energy resolution parameter  $a_{res}$ .

#### 4.4 Impact of Electron and Positron Polarisation

To exploit the full physics potential of a linear collider, electron and positron beams will be polarised. Polarisation will also change the Bhabha cross section in the acceptance range of LumiCal up to a few per cent [29]. In the current design the maximum values for electron and positron polarisation are 0.8 and 0.6, respectively, with an uncertainty of 0.0025 [30]. Using these values the shift in the Bhabha cross section is  $2.3 \times 10^{-2}$  with an uncertainty of  $1.9 \times 10^{-4}$ .

#### 4.5 Summary of Systematic Uncertainties

In addition to effects studied in this chapter also the impact of the polar angle resolution and polar angle bias as estimated in section 2.1 are included. All uncertainties based on the current level of understanding are summarised in Table 2. They are considered as being uncorrelated, leading currently to a total uncertainty of  $2.3 \times 10^{-3}$ . The reduction of the largest uncertainty due to the uncertainty of the luminosity spectrum needs further investigation. The energy scale uncertainty and the energy resolution uncertainty may be reduced by a proper calibration.

### 5. Sensor Development

#### 5.1 BeamCal

The challenge of BeamCal is to find sensors tolerating about a MGy of dose per year. So far polycrystalline CVD<sup>1</sup> diamond sensors of  $1 \text{ cm}^2$  size and larger sectors of GaAs pad sensors, as shown in Figure 14, have been studied. Irradiation studies are done using a 10 MeV electron beam at the sDALINAC accelerator [31]. Varying the intensity between 10 and 100 nA corresponding to dose rates of 10 to 200 kGy/h. Since large area CVD diamond sensors are extremely expensive,

<sup>1</sup>Chemical Vapor Deposition

source	Value	Uncertainty	luminosity uncertainty
$\sigma_\theta$	$2.2 \times 10^{-2}$	100%	$1.6 \times 10^{-4}$
$\Delta_\theta$	$3.2 \times 10^{-3}$	100%	$1.6 \times 10^{-4}$
$a_{\text{res}}$	0.21	10%	$3 \times 10^{-4}$
luminosity spectrum			$1.5 \times 10^{-3}$
bunch sizes $\sigma_x, \sigma_z$ ,	100nm, $300 \mu\text{m}$	5%	$10^{-3}$
two photon events	$2.3 \times 10^{-3}$	40%	$0.9 \times 10^{-3}$
energy scale		400 MeV	$10^{-3}$
polarisation, $e^-, e^+$	0.8, 0.6	0.0025	$1.9 \times 10^{-4}$
total uncertainty			$2.3 \times 10^{-3}$

Table 2:

The estimated systematic uncertainties on the luminosity measurement from all sources considered above at a centre-of-mass energies of 500 GeV.

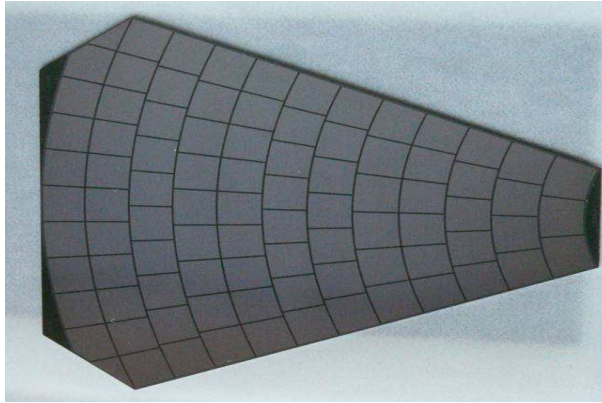


Figure 14: A prototype of a GaAs sensor sector for BeamCal with pads of about  $30 \text{ mm}^2$  area.

they may be used only at the innermost part of BeamCal. At larger radii GaAs sensors appear to be a promising option.

### 5.1.1 GaAs Sensors

Large area GaAs sensors are obtained from the Siberian Institute of Technology. They are produced using the liquid encapsulated Czochralski method and are doped with tin and tellur as shallow donors and chromium as a deep acceptor.

Three batches with different concentrations of dopants are irradiated up to 1.2 MGy and the charge collection efficiency, CCE, is measured as a function of the absorbed dose. For all sensors a MIP signal is separated from the pedestal up to a dose of 600 kGy. The charge collection efficiency depends slightly on the dopant concentration. The sensors with a lower donor concentration show a larger initial charge collection efficiency and the decrease of the charge collection efficiency as a

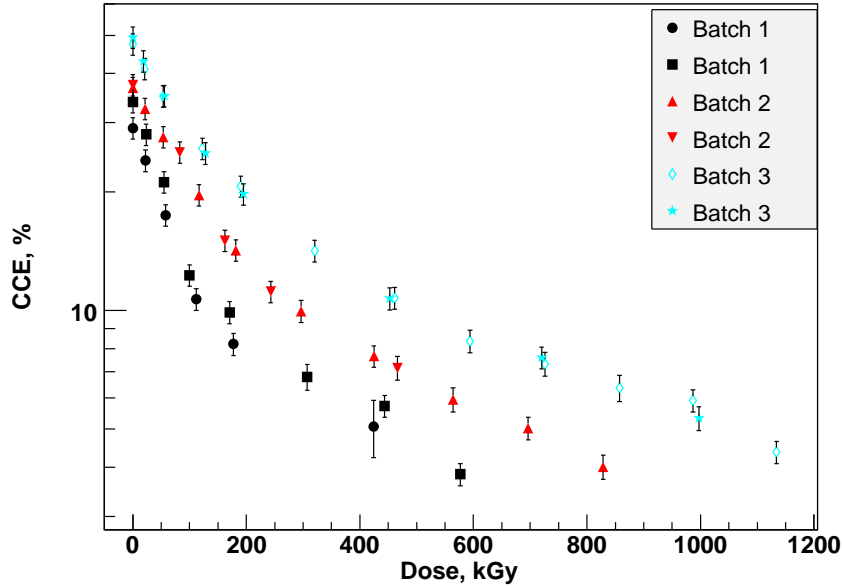


Figure 15: The CCE as a function of the absorbed dose for the GaAs sensors with different donor concentrations. The donor is Te for the batches 1 and 2 and Sn for batch 3.

function of the absorbed dose is less steep, as can be seen in Figure 15. The leakage current of a pad at room temperature before irradiation is about 500 nA at an applied voltage of 100 V. After irradiation the leakage current approaches 1  $\mu$ A. The pad capacitance is measured to 12 pF. The results are consistent with previous measurements [32].

### 5.1.2 CVD Diamond Sensors

For polycrystalline diamond sensor samples the linearity of the response and the the leakage current and the signal collection efficiency have been investigated as a function of the absorbed dose [34]. The signal size depends linearly on the number of charged particles crossing the sensors for up to  $5 \times 10^6$  particles in 10 ns. The leakage current at room temperature depends only slightly on the absorbed dose up to doses of 7 MGy. The charge collection efficiency rises by a factor of two for doses between 0.5 to 1 MGy, then drops smoothly approaching the charge collection efficiency of a non-irradiated sensor. Provided the sensor is continuously irradiated, this efficiency is reached at about 7 MGy.

## 5.2 Sensors for LumiCal

Prototypes of LumiCal sensors have been designed [33] and then manufactured by Hamamatsu Photonics. A picture of a sensor is shown in Figure 16. Its shape is a ring segment of  $30^\circ$ . The thickness of the n-type silicon bulk is 320  $\mu$ m. The pitch of the concentric  $p^+$  pads is 1.8 mm and the gap between two pads is 0.1 mm. The leakage current of a single pad as a function of the bias voltage is shown in Figure 17a. Putting the neighboring pads on ground stabilizes the measurement and reduces the current values by a factor of two. The leakage currents of all the pads of one sensor

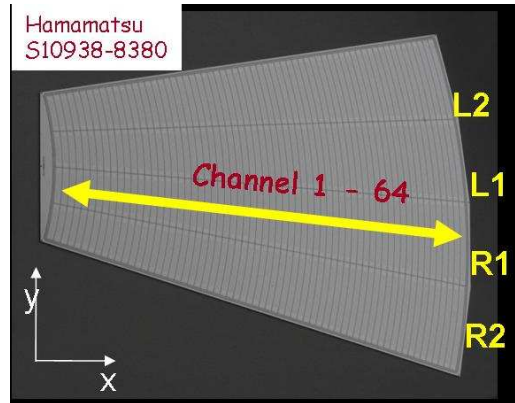


Figure 16: A prototype silicon sensor for LumiCal

have been measured at a bias voltage of 500 V. All pads except one have a leakage current in the range from 1 to 4 nA. Less than 5% of all pads have a break-through voltage below 500 V. For other sensors the results are similar. The capacitance as a function of the bias voltage for a pad is shown

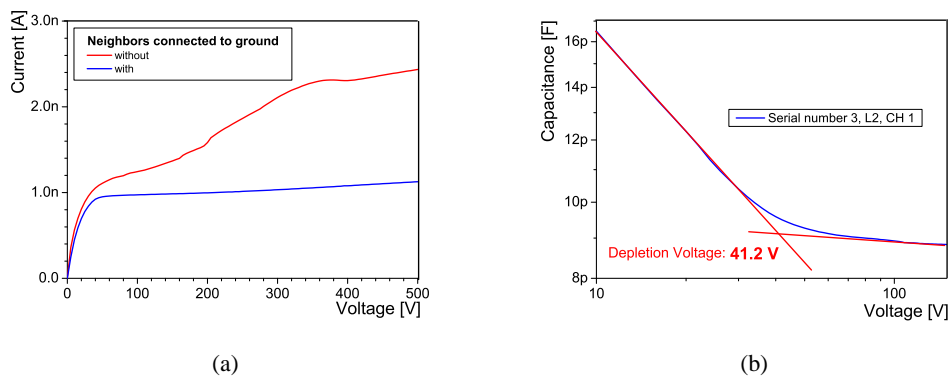


Figure 17: (a) The dependence of the leakage current on the bias voltage for a single pad with and without grounded neighbors. (b) The capacitance of a pad as a function of the bias voltage.

in Figure 17b. At a voltage of 150 V the pad capacitance values are 25 pF for the largest pads and 10 pF for the smallest pads, respectively. Also shown is how the value of the full depletion voltage is obtained. Values from 39 V to 43 V were found.

## 6. ASIC Developments

new particle

### 6.1 LumiCal Readout

The design of the LumiCal front-end electronics is done for the proposed detector architecture [35]. The front-end ASIC should work in two modes: the physics mode and the calibration mode. In the physics mode electromagnetic showers will be measured with large energy depositions on the

pads. The front-end ASIC should process signals up to at least 6 pC per channel. In the calibration mode MIP-like signals from single relativistic muons should be measured. The minimum size of these signals is 2 fC, corresponding to low end of the Landau distribution for MIPs in 300  $\mu\text{m}$  thick silicon. The proposed sensor geometry results in a range of pad capacitances between 10 pF and, considering also the readout pads, 100 pF. Because of the high expected occupancy, the front-end ASIC should be fast enough to resolve signals from subsequent bunch crossings which are separated in time by about 300 ns.

The simulations of LumiCal indicate that the shower reconstruction needs at least 8 bit precision. Severe requirements are set on the readout electronics power dissipation may be strongly relaxed if switching of the power between bunch trains is done. This is feasible since in the ILC experiments after each 1 ms bunch train there will be about 200 ms pause [12].

To fulfil the above specifications the general concept of the full readout chain comprising a front-end electronics, a digitiser (ADC) plus zero suppression and a data concentrator with optical driver is chosen. One ADC may serve for one or for more channels. In the following the design and the measurements of prototypes of front-end and the ADC ASICs are presented.

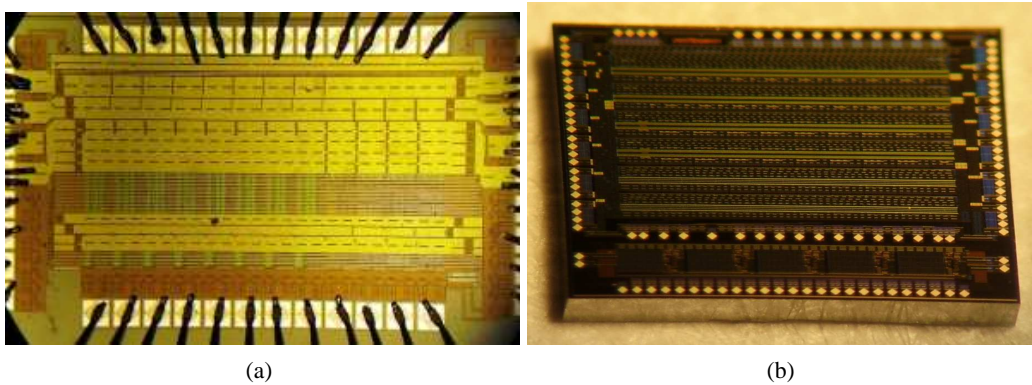


Figure 18: (a) Photograph of prototypes of the front-end ASIC and (b) the ADC ASIC

The prototype ASICs, as shown in Figures 18a and 18b, are fabricated in 0.35  $\mu\text{m}$  CMOS technology. A more detailed discussions of the front-end ASICs can be found in Ref. [36] and of the ADC ASICs in Ref. [37].

### 6.1.1 Front-end Electronics Design

The chosen front-end architecture comprises a charge sensitive amplifier, a pole-zero cancellation circuit (PZC) and a shaper, as shown in Figure 19. In order to cope with large charges in the physics mode and small ones in the calibration mode a variable gain in both the charge amplifier and the shaper is applied. The mode switch in Figure 19 changes effective values of the feedback circuit components  $R_f$ ,  $C_f$ ,  $R_i$ ,  $C_i$  and so changes the transimpedance gain of the front-end ASIC. The low gain (large  $C_f$ ) is used for the physics mode when the front-end processes signals from large charge depositions in the sensor, while the high gain (small  $C_f$ ) is used in the calibration mode. Assuming high enough open loop gain of the pre-amplifier ( $A_{\text{pre}}$ ) and the shaper amplifier ( $A_{\text{sh}}$ ), the transfer

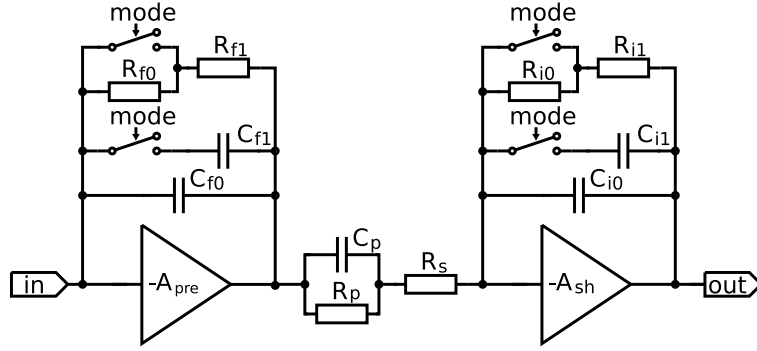


Figure 19: Block diagram of the single front-end channel

function of this circuit is given as:

$$\frac{U_{out}(s)}{I_{in}(s)} = \frac{1}{C_f C_i R_s} \cdot \frac{s + 1/C_p R_p}{s + 1/C_f R_f} \cdot \frac{1}{(s + 1/C_i R_i)(s + 1/C_p(R_p || R_s))}. \quad (6.1)$$

Setting properly the PZC parameters ( $C_f R_f = C_p R_p$ ) and equalising shaping time constants ( $C_i R_i = C_p(R_p || R_s)$ ) one obtains the first order shaping, equivalent to a CR-RC filter, with a peaking time  $T_{peak} = C_i R_i$ . A simple first order shaping is chosen as a tradeoff between the noise and the power dissipation. Regarding the noise a main requirement is to obtain in calibration mode the signal to noise ratio (S/N) of about 10 for the largest sensor capacitances. Both of the amplifying stages ( $A_{pre}, A_{sh}$ ) are designed as the folded cascodes [38] with active loads, followed by the source followers. In the prototype ASIC 8 front-end channels are implemented.

### 6.1.2 Front-end Electronics Measurements

Figure 20a shows the response of the front-end channel to charge injected through the input test capacitance for different values of input capacitance ( $C_{det}$ ) within the interesting range. The sensor capacitance is simulated with an external capacitor. It is seen that both, the amplitude and the peaking time ( $\sim 70$  ns), are not sensitive to the value of the input capacitance in agreement with hspice simulations.

The output noise has been measured using a HP3400 true rms meter. The equivalent noise charge (ENC) as a function of input capacitance is shown in Figure. 20b. Results obtained for the physics and calibration modes are shown on the same plot. Since the HP3400 bandwidth is only up to 10 MHz the numbers may be underestimated by about 20%. The ENC vs  $C_{det}$  behaviour and the measured values are generally in agreement with simulations. In particular, in the calibration mode the signal to noise ratio of 10 is maintained for input capacitances up to about 100 pF. For a few points additional noise measurements have been performed by measuring the output noise spectra using a HP4195A spectrum analyser and then integrating it numerically. The results of such measurements are added in Figure 20b. They agree within their uncertainties with the HP3400 measurements.

In order to test the effectiveness of the PZC circuit the front-end response has been measured as a function of the rate of input pulses. To avoid input charges of both polarities when

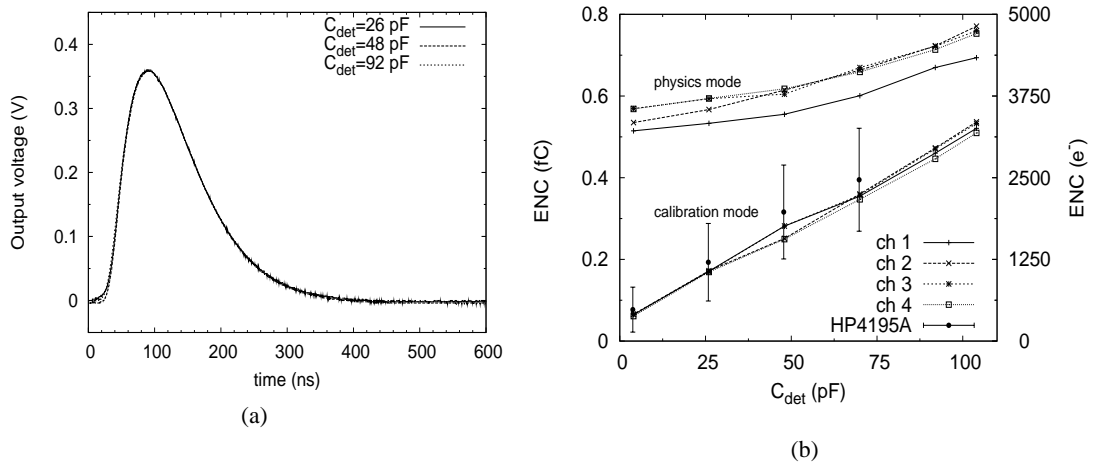


Figure 20: (a) Output pulses in physics mode as a function of the input capacitance for  $Q_{in}=3.3$  pC (b) Noise ENC measurements obtained with true rms meter for the front-end ASIC with passive feedback

using a square-wave test signal, the staircase test waveforms are synthesised using the Tektronix AWG2021 waveform generator. It was found that the change in amplitude reaches 2% for input rates of about 3 MHz and is almost not sensitive to the input capacitance. The power consumption of about 8.9 mW/channel is measured what confirms well the simulations.

### 6.1.3 ADC Design

As a compromise between speed, area and power consumption the ADC was designed using pipeline technology. A 1.5-bit per stage architecture is chosen because of its simplicity and immunity to the offsets in the comparator and amplifier circuits. The prototype ADC consists of an input sample and hold (S/H) circuit, 9 pipeline stages and digital correction circuitry. In addition the power switching feature is also implemented.

### 6.1.4 ADC Performance Measurements

The static measurements of the Integral Nonlinearity, INL, and the Differential Nonlinearity, DNL, obtained at a sampling frequency of 20 MHz, are shown in Figures 21a and Figures 21b. These parameters are calculated using the histogramming method. The measured INL is always less than 1 LSB while the DNL is below 0.5 LSB. These results attest to very good ADC linearity. To estimate the dynamic performance measurements with sinusoidal wave input are performed [39]. An example of a measured spectrum using a 1.8 MHz full scale (0 dB) input signal sampled at 20 MHz is shown in Figure 22a. It is seen that the noise and harmonic components are small enough not affecting significantly the resolution. The signal to noise ratio, SNHR, is measured as a function of sampling frequency as shown in Figure 22b. An SNHR of about 58 dB is obtained in the frequency range up to almost 25 MHz.

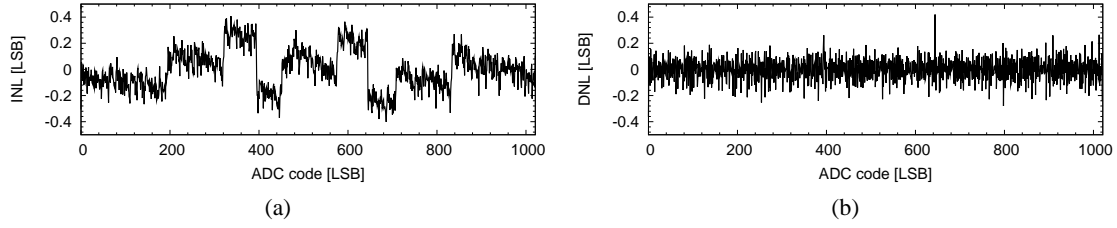


Figure 21: Static measurements of (a) INL and (b) DNL errors at 20 MHz sampling frequency

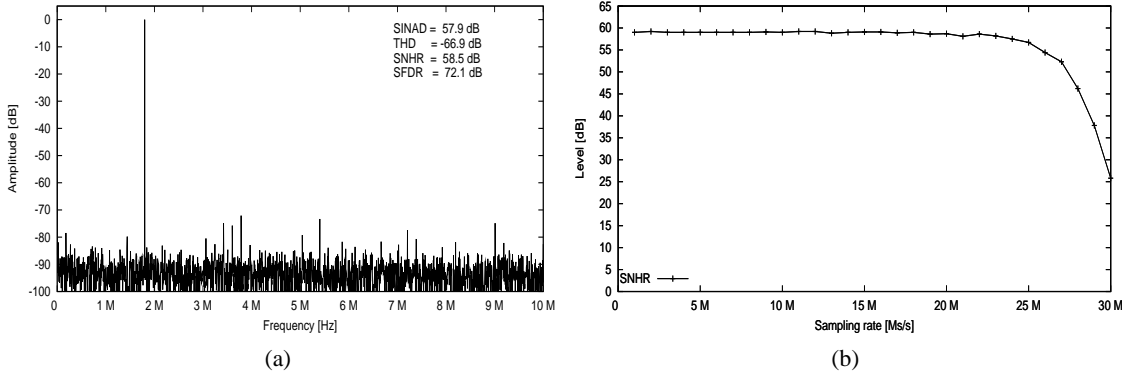


Figure 22: (a) Example of FFT measurement with  $f_{in}=1.8$  MHz and  $f_{clk}=20$  MHz, (b) ADC performance as a function of the sampling rate

## 6.2 BeamCal Front-End ASIC Development

The BeamCal ASIC, designed for 180-nanometer TSMC technology, will be able to handle 32 channels. The two modes of operation require a front-end circuit capable of a wide performance envelope: high slew rate for standard data taking, and low noise for calibration. In standard data taking the occupancy is high, and therefore all data from a full bunch train must be recorded, to be read out between bunch trains. Because of its reliability, density and redundancy possibilities, a digital memory array will be used to store the data from all collisions in each bunch train. This choice requires a sampling rate of 3.25MHz per channel, which is achieved by 10-bits, successive approximation analog-to-digital converters [40]. The small size of this ADC architecture allows to use one converter per channel.

In this front-end ASIC, the dominant noise source is the charge sensitive amplifier series noise. Assuming 40 pF input capacitance, high occupancy and the 300 ns period make it necessary a careful design of noise filtering and baseline restoration [41].

In order to take advantage of all the time available for signal processing, the filter for calibration operation has been implemented using switched-capacitor, SC, circuits [42]. This technique allows to precisely define the circuit time constants depending on the input clock frequency and the ratio of two capacitors. Baseline restoration is achieved by means of a fast gated reset, followed by a slow reset-release technique to reduce the effect of a split doublet. The slow reset-release is implemented using SC circuits.

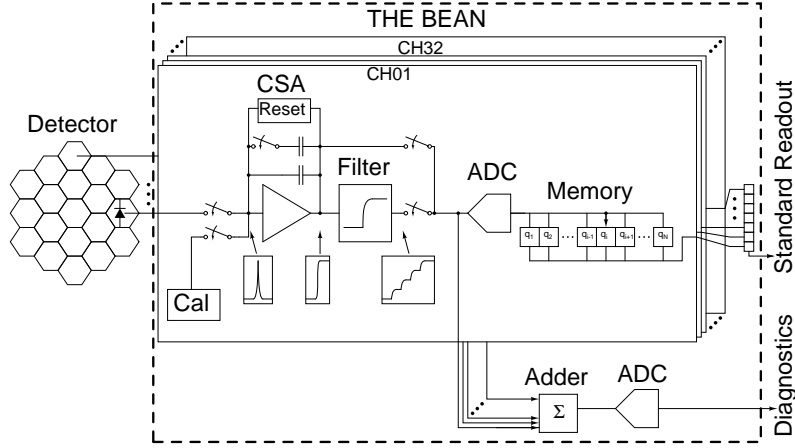


Figure 23: Simplified BeamCal ASIC block diagram of a single channel

In standard data taking operation, an adequate noise power is effectively achieved by means of a slow reset-release technique, similar to that used in calibration operation. An explicit filter for standard data taking operation is unnecessary, as the amplifier bandwidth suffices for noise filtering purposes.

Figure 23 shows a simplified block diagram for a single channel. In standard data taking operation, since it is unnecessary for filtering, the integrator is bypassed to reduce power consumption.

For design purposes, the transistor-level noise analysis has been carried out using the  $g_m/I_D$  technique [43], which takes noise coefficients directly from SPICE simulation results. As this is a gated front-end, the system-level noise analysis has been done using the weighting function approach.

Since the system's dominant noise source is series noise, a triangular-shaped weighting function effectively minimizes the output noise power. The negative slope section of the triangular weighting function is easily implemented by means of an integrator – in this case, a SC integrator. The positive slope section is achieved by means of the slow reset-release technique mentioned earlier. The weighting function resulting from an ideal reset-release and a SC integrator is shown in Figure 24, left; a more realistic weighting function, reconstructed from SPICE simulation results, is shown in the right pane. In both cases, the target noise level is effectively achieved.

### 6.2.1 Circuit Implementation

The charge sensitive amplifier is a folded-cascode amplifier with NMOS input device, connected to a switched-capacitor feedback network. The amplifier input transistor is biased at  $450 \mu\text{A}$  whereas the load works at about  $50 \mu\text{A}$ . The feedback network consist of two feedback capacitors of  $0.9 \text{ pF}$  and  $44.1 \text{ pF}$  for calibration and standard data taking modes, respectively. Both have a reset transistor, with a gate voltage driven by the switched-capacitor reset-release network. The amplifier output is pseudo-differential.

In order to isolate the amplifier from the filter's SC-related kickback noise, a buffer circuit is used. The buffer also allows signal shifting, producing a more adequate common-mode level for the filter. The buffer consumes  $130 \mu\text{A}$  and consists of a source follower, with cascoded current

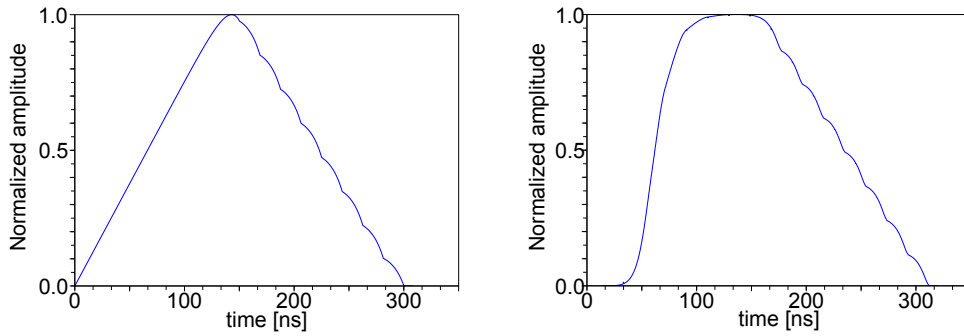


Figure 24: Front-end weighting function assuming ideal components (left) and simulation results (right) in the calibration mode

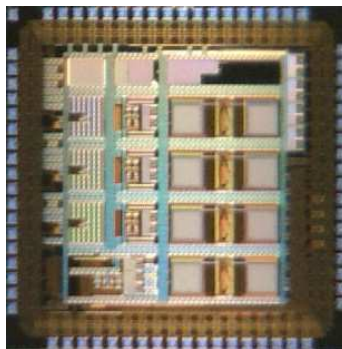


Figure 25: BeamCal Instrumentation ASIC Prototype

source and an additional device to keep a nearly constant  $V_{DS}$  in the input transistor. This serves the purpose of enhancing the buffer linearity.

The filter implemented is a fully-differential switched-capacitor integrator. Capacitor values were carefully designed in order to obtain the adequate noise performance. The core of the integrator is a class A/AB amplifier [44] that consumes  $456 \mu A$ .

The converter is a 10-bit, fully-differential successive approximation register ADC. The one included in the BeamCal ASIC has 16 fF unit capacitances, and similar versions with 4 fF and 2 fF unit capacitances were also designed for individual characterization.

The BeamCal ASIC prototype, similar to the ASIC described in Figure 23, but including only three channels and no internal memory, was fabricated and is currently being tested. Figure 25 shows the  $2.4 \text{ mm} \times 2.4 \text{ mm}$  die.

## 6.2.2 Test Results

The ADC in the BeamCal ASIC has been quantitatively characterized, along with the additional versions of the ADC using smaller unit capacitances. All the linearity measurements have shown excellent results. Figures 26a and 26b show the INL and DNL for the ADC using 2 fF capacitors. The results are consistent with unit capacitance matching better than 0.1%. The INL cubic-like

shape in Figure 26a is explained due to copper dishing effects, and will be corrected in future versions by re-arranging the capacitor array connections.

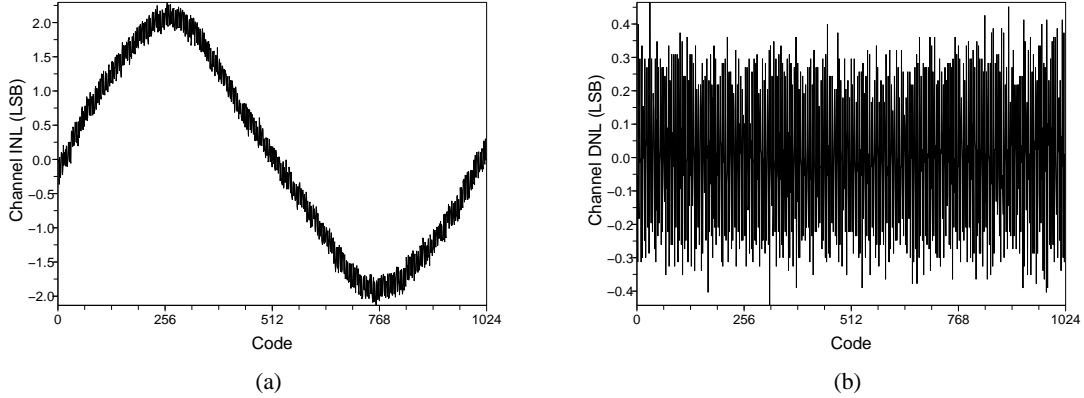


Figure 26: Results of (a) the INL and (b) the DNL errors using 2 fF unit capacitors.

### 6.3 Pair Monitor

A prototype ASIC has been designed with 36 readout cells arranged as an array of 6 x 6, as shown in Figure 27. Each cell has an amplifier block, comparator, 8-bit counter and 16 count-registers. The amplifier block consists of charge sensitive pre-amplifier, threshold block and differential-amplifier. The pre-amplifier is a constant-current feedback-type amplifier. The time-over-threshold of the output signal is proportional to the injected charge through the constant current feedback in the pre-amplifier. In the 8-bit counter, the gray code is used to count the number of hits. The 16 count-registers are prepared to store hit counts in one bunch train subdivided in 16 time slices. There are also decoders which select a count-register to store and readout the hit count. A shift register to select a readout pixel, data transfer to the output line and distributor of the operation signals are arranged around the 36 readout cells as a glue logic. The bonding pad is prepared in each cell to be attached to a sensor with bump bonding. The prototype ASIC has been produced with TSMC 0.25- $\mu\text{m}$  CMOS process. The chip size is  $4 \times 4 \text{ mm}^2$ , and the readout cell size is  $400 \times 400 \mu\text{m}^2$ . The chip was packaged in PGA144 for the operation tests.

Figure 28 shows the response of the counter block. The state of the counter bits changes at each test pulse indicating a bunch crossing. The number of hits is measured in 16 time slices of a bunch train. The data stored will then read out during the inter-train time. The test is performed counting the hits in each time slice with a count rate is set to 4 MHz, larger than expected at the ILC. The number of hits was counted without any bit lost.

We also studied the noise level in the circuit. The count efficiency was investigated as a function of the threshold voltage at the comparator. Fitting the efficiency curve with the error function, a standard deviation of 0.94 mV was obtained. With the gain of  $1.6 \times 10^{-3} \text{ mV}$  per electron, this corresponds to an ENC of about 600 electrons.

As the next step, a pair-monitor prototype will be built in Silicon On Insulator technology. The sensor and readout ASIC will be prepared on the same wafer. This prototype will be used to

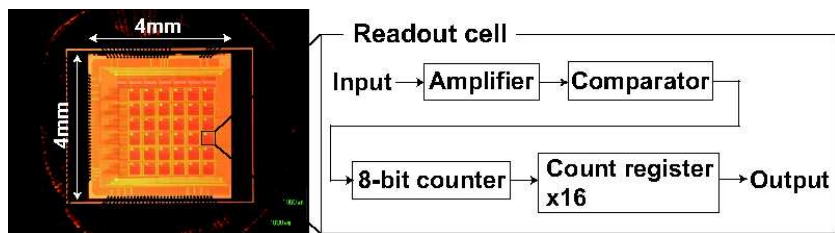


Figure 27: Picture of the prototype of the pair monitor readout ASIC and schematic diagram of the circuit in a readout cell. The readout cell consists of the amplifier, comparator, 8-bit counter, and 16 count-registers.

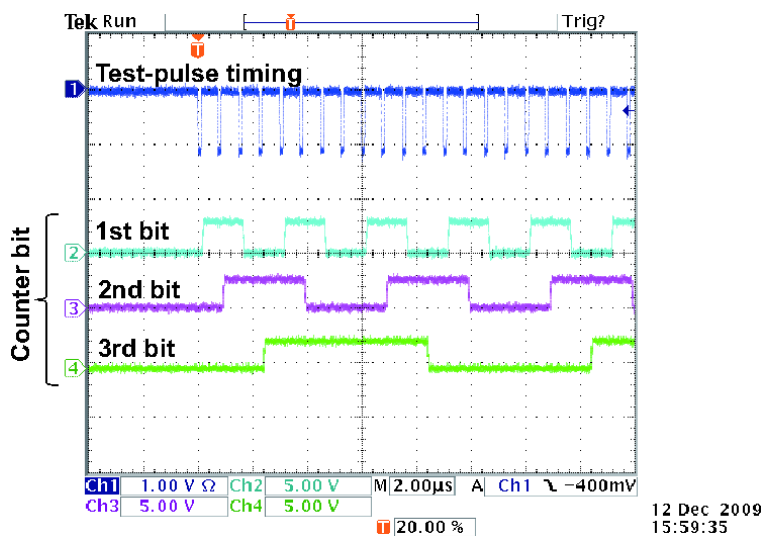


Figure 28: Output signals from the counter block. The lower 3 bits of the 8-bit counter are shown. The test-pulse timing corresponds to the bunch crossing frequency if the ILC.

investigate apart of the standard characteristics also the radiation tolerance. Currently, an ASIC is developed in OKI 0.2  $\mu\text{m}$  FD-SOI CMOS technology.

## 7. Acknowledgments

This work is supported by the Commission of the European Communities under the 6<sup>th</sup> Framework Program "Structuring the European Research Area", contract number RII3-026126. Tsukuba University is supported in part by the Creative Scientific Research Grant No. 18GS0202 of the Japan Society for Promotion of Science. The UST is supported by the Polish Ministry of Science and Higher Education under contract Nr. 372/6.PRUE/2007/7. The INP PAN is supported by the Polish Ministry of Science and Higher Education under contract Nr. 141/6.PR UE/2007/7 IFIN-HH is supported by the Romanian Ministry of Education, research and Innovation through the Authority CNCISIS under contract IDEI-253/2007. This study has been carried out within the project "Physics and Detector R&D in HEP Experiments" supported by the Ministry of Science of the Republic of

Serbia. J. Aguilar, P. Ambalathankandy and O. Novgorodova are supported by the 7th Framework Programme "Marie Curie ITN", grant agreement number 214560.

## References

- [1] H. Abramowicz *et al.*, *Instrumentation of the very forward region of a linear collider detector*, *IEEE Trans.Nucl.Sci.* **51** (2004) 2983.
- [2] T. Abe *et al.*, *The International Large Detector: Letter of Intent*, FERMILAB-LOI-2010-01, FERMILAB-PUB-09-682-E, DESY-2009-87, KEK-REPORT-2009-6, arXiv:1006.3396.
- [3] K. Mönig, *Physics Needs for the Forward Region, V. Workshop: Instrumentation of the Forward Region of a Linear Collider Detector*, August, 26–28, 2004 DESY, Zeuthen, Germany, .
- [4] Ch. Grah and A. Saproinov, *Beam parameter determination using beamstrahlung photons and incoherent pairs*, 2008 *JINST* **3** P10004.
- [5] S. Jadach *et al.*, *BHWIDE 1.00: O(alpha) YFS exponentiated Monte Carlo for Bhabha scattering at wide angles for LEP1/SLC and LEP2*, *Phys. Lett.*, **B390**, (1997), 298-308.
- [6] S. Agostinelli *et al.*, *Geant4- a simulation toolkit*, *Nucl. Inst. and Meth.A* **506** (2003) 250.
- [7] *MOKKA, A simulation program for linear collider detectors.*
  
- [8] T. C. Awes *et al.*, *A simple method of shower localization and identification in laterally segmented calorimeters*, *Nucl. Inst. Meth. A* **311**, (1992), 130.
- [9] I. Sadeh, *Luminosity Measurement at the International Linear Collider*, , 2008.
- [10] H. Abramowicz *et al.*, *Redefinition of the Geometry of the Luminosity Calorimeter*, *EUDET-Memo-2008-09*, 2008, .
- [11] H. Abramowicz *et al.*, *Revised Requirements on the Readout of the Luminosity Calorimeter*. *EUDET-Memo-2008-08*, 2008, .
- [12] J. Brau *et al.*, *ILC Reference Design Report*, , 2007.
- [13] D. Schulte, *Beam-beam simulations with guinea-pig*, *CERN-PS-99-014LPCLIC-Note* 387, 1998.
- [14] A. Seryi *et al.*, *IR OPTIMIZATION AND ANTI-DID*, *SLAC-PUB-11662*, 2006.
- [15] P. Bambade *et al.*, *The Impact of Beamcal Performance at Different ILC Beam Parameters and Crossing Angles on stau Searches*, *Pramana J. Phys.* 69 (2007) 1123.
- [16] A. Heikkinen and N. Stepanov, *Bertini Intra-nuclear Cascade implementation in Geant4*, *Proceedings of CHEP03*, La Jolla, California, 2003, nucl-th0306008.
- [17] C. Coca *et al.*, *Rom. J. Phys.*, 2010, *in press*.
- [18] T. Tauchi *et al.*, *Nanometer Beam-Size Measurement during Collisions at Linear Colliders*, *KEK preprint* **94-122** 1995.
- [19] T. Tauchi *et al.*, *Pair creation from beam-beam interaction in linear colliders*, *Particle Accelerator* **41**,(1993), 29.
- [20] K.Ito, *Study of Beam Profile Measurement at Interaction Point in International Linear Collider*, *arXiv: 0901.4151[physics.ins-det]*

- [21] A. Elagin, *The Optimized Sensor Segmentation for the Very Forward Calorimeter*, *Proceedings of the 2005 International Linear Collider Physics and Detector Workshop*, Snowmass, Colorado, 2005, ECONF C0508141:ALCPG0719.
- [22] J. Blocki *et al.*, *LumiCal new mechanical structure*, *EUDET-Memo-2009-10*, .
- [23] C. Rimbault *et al.*, *Impact of beam-beam effects on precision luminosity measurements at the ILC*, 2007 *JINST* **2** P09001.
- [24] W. Kilian. *WHIZARD: A generic Monte-Carlo integration and event generation package for multi-particle processes*, LC-TOOL-2001-039, 2001.
- [25] V. N. Pozdnyakov, *Two-photon interactions at LEP*, *Phys. Part. Nucl. Lett.*, **4** (2007), 289-303.
- [26] S. Jadach *et al.*, *Monte Carlo program BHLUMI for Bhabha scattering at low polar angle with Yennie-Frautschi-Suura exponentiation*, *Comp. Phys. Commun.*, **70** (1992), 305-344.
- [27] B. Pawlik, *BARBIE V4.3 Easy-to-use-simulation-package of the TESLA LAT Detector*, source available from Bogdan.Pawlik@ifj.edu.pl.
- [28] I. Smiljanic *et al.*, *TOWARDS A FINAL SELECTION FOR LUMINOSITY MEASUREMENT*, *Proceedings of the Workshop of the Collaboration on Forward Calorimetry at ILC (2008)*, Belgrade Serbia, B. Pawlik, private communication.
- [29] Ch. Grah *et al.*, *Report to the Detector R&D Panel Instrumentation of the Very Forward Region*, , 2007.
- [30] S. Boogert *et al.*, *Polarimeters and Energy Spectrometers for the ILC Beam Delivery System*, 2009 *JINST* **4** P10015.
- [31] *S-DALINAC: Superconducting DArmstadt Llinear ACcelerator*,
- [32] Ch. Grah *et al.*, *Radiation hard sensor for the BeamCal of the ILD detector*, *Proceedings of the IEEE conference*, October 27 – November 3 2007 Honolulu, USA.
- [33] J. Blocki *et al.*, *Silicon Sensors Prototype for LumiCal Calorimeter*, *EUDET-Memo-2009-07*.
- [34] Ch. Grah *et al.*, *Polycrystalline CVD Diamonds for the Beam Calorimeter of the ILC*, *IEEE Trans.Nucl.Sci.* **56** (2009) 462.
- [35] M. Idzik *et al.*, *Status of VFCAL*, *EUDET-memo-2008-01* (2008).
- [36] M. Idzik *et al.*, *Development of front-end electronics for the luminosity detector at ILC*, *Nucl. Instr. and Meth., A* **608** (2009), 169-174.
- [37] M. Idzik *et al.*, *Development of a Pipeline ADC for the Luminosity Detector at ILC*, *Proceedings of the 15th International Conference "Mixed Design of Integrated Circuits and Systems" MIXDES 2008*, Poznan, Poland, 19-21 June 2008.
- [38] E. Beuville *et al.*. *AMPLEX, a low-noise, low-power analog CMOS signal processor for multielement silicon particle detectors*, *Nucl. Instr. and Meth., A* **288a** (1990), 157-167.
- [39] *IEEE standard for terminology and test methods for analog-to-digital converters*, *IEEE-STD-1241* (2000).
- [40] J.L. McCreary and P.R. Gray, *All-MOS charge redistribution analog-to-digital conversion techniques. I. Solid-State Circuits*, *IEEE Journal of*, 10(6), (1975), 371–379.

- [41] H. Spieler, *Semiconductor Detector Systems*. Oxford University Press, 2005.
- [42] R. Gregorian, K.W. Martin, and G.C. Temes, *Switched-capacitor circuit design*, *Proceedings of the IEEE*, 71(8), (1983),941–966.
- [43] F. Silveira, D. Flandre, and P.G.A. Jespers, *A  $g_m/I_D$  based methodology for the design of CMOS analog circuits and its application to the synthesis of a silicon-on-insulator micropower OTA*. *Solid-State Circuits, IEEE Journal of*, 31(9), (1996), 1314–1319.
- [44] S. Rabbii, *Design of Low-Voltage Low-Power Sigma-Delta Modulators*, *PhD thesis, Stanford University*, 1998.